Research Square

Preprints are preliminary reports that have not undergone peer review.
They should not be considered conclusive, used to inform clinical practice,
or referenced by the media as validated information.

# Compositionally Graded Additive Manufacturing: A Method for Alloy Development and Tribocorrosion Evaluation

**Scott M. Wells**

swells@goprecise.com

Excet, A Precise Systems Company

**Mary E. Parker**

United States Naval Research Laboratory

**Anna K. Rawlings**

United States Naval Research Laboratory

**Andrew J. Birnbaum**

United States Naval Research Laboratory

**Method Article**

**Keywords:**

**Posted Date:** November 12th, 2026

**DOI:** https://doi.org/10.21203/rs.3.rs-11512502/v1

**License:** This work is licensed under a Creative Commons Attribution 4.0 International License.
Read Full License

**Additional Declarations:** No competing interests reported.

# Compositionally Graded Additive Manufacturing: A Method for Alloy Development and Tribocorrosion Evaluation

Scott M. Wells [1]*, Mary E. Parker[2], Anna K. Rawlings[3], Andrew J. Birnbaum[3]

[1]*Excet, A Precise Systems Company, Lexington Park, MD 20653, USA*

[2]*Chemistry Division, Code 6130, U.S. Naval Research Laboratory, Washington, DC 20375, USA*

[3]*Materials Science and Technology Division, Code 6300, U.S. Naval Research Laboratory, Washington, DC 20375, USA*

*Corresponding author: swells@goprecise.com

## Abstract

Additive manufacturing (AM) enables the fabrication of materials with tailored compositional and microstructural gradients, offering unique opportunities for studying complex degradation phenomena such as tribocorrosion. In this work, a thin-walled stainless steel build with a continuous compositional gradient from super-austenitic AL6XN to austenitic 316L was produced using a dual-hopper powder feed system. Energy-dispersive spectroscopy (EDS) confirmed the compositional gradient and corresponding decrease in pitting resistance equivalent number (PREN), while electron backscatter diffraction (EBSD) revealed a microstructural gradient characteristic of thin-walled AM builds, evolving from fine elongated grains near the baseplate to coarser columnar grains at the top. Potentiostatic tribocorrosion testing in 0.6 M NaCl under anodic applied potentials demonstrated that wear rate increased with build height, inversely following the PREN gradient. Microhardness measurements confirmed the additional contribution of microstructural evolution on the local wear resistance which also impacts tribocorrosion performance. Current transients showed higher dissolution activity in 316L-rich regions and lower currents in AL6XN-rich regions, consistent with SEM observations of increased corrosion products in the 316L-regions. These results highlight that tribocorrosion performance is driven by the combined effects of wear resistance and corrosion resistance. More importantly, they demonstrate the utility of AM-graded samples as an efficient platform for screening alloys enabling novel alloy development and as a means for probing the coupled effects of wear and corrosion in tribocorrosion studies.

## 1. Introduction

### 1.1 Tribocorrosion of Corrosion Resistant Alloys

Tribocorrosion, or wear-enhanced corrosion, is a well-recognized but complex phenomenon whereby mechanical wear and electrochemical degradation occur simultaneously. A key barrier to understanding tribocorrosion mechanisms is the inherently coupled nature of these processes (wear and corrosion), as treating them independently does not fully account for the degradation observed during tribocorrosion. Experimental evidence consistently demonstrates that wear can accelerate



Distribution Statement A: Approved for public release. Distribution is unlimited.

corrosion by disrupting passive films, while corrosion can amplify wear by compromising surface integrity. In an effort to quantify this interplay, various methods have been proposed including synergistic, mechanistic, and third-body approaches, as well as through complex mathematical models. These approaches lie outside the scope of this work, but their common conclusion underscores the necessity of considering wear and corrosion as interdependent processes when assessing material performance in tribocorrosion environments.

Several approaches are available to evaluate tribocorrosion performance including potentiostatic and potentiodynamic testing. A comprehensive review by Mischler summarized the advantages and limitations of these techniques. Potentiostatic testing is most commonly employed because the application of a constant potential facilitates quantification of current transients associated with depassivation and repassivation events during wear, while also ensuring high reproducibility. The two primary experimental configurations are the unidirectional pin- or ball-on-disk method, in which a loaded counterbody slides against a rotating sample to generate a circular wear pattern, and the bidirectional pin- or ball-on-plate method, where the counterbody reciprocates across the sample to form a linear wear track. Numerous studies are available in the literature demonstrating both the pin/ball-on-disk and the pin/ball-on-plate methods for steel alloys.

### 1.2 Compositional Gradient for Alloy Development

Additive manufacturing (AM) is a fabrication technique first developed in the mid-1980s in which a feedstock material, typically supplied as a wire or powder (either blown or bedded), is selectively melted using a focused heat source such as a laser or electron beam. Through repeated melting passes, this process enables the layer-by-layer construction of components at fine length scales. Recently, AM has received increasing research attention as its unique production strategy allows for the fabrication of geometries and material systems that are challenging or even impossible to achieve using conventional casting techniques. One area of interest in particular is the rapid development of novel alloys. Traditionally, alloy discovery has relied on full-scale research castings or diffusion couples, as demonstrated by Marceau et. al., to more efficiently sample broader compositional spaces. Although compositional thermodynamics has advanced rapidly and now plays a central role in alloy design, experimental validation through casting remains arduous. Certain metal AM techniques offer an alternative by enabling the fabrication of components with spatially varying compositions, thus accelerating the exploration of untested alloys, as highlighted in the review by Hofmann et. al..

Several recent studies illustrate the use of AM in alloy development. Fischer et. al. investigated a binary titanium-niobium alloy for biomedical applications using selective laser melting (SLM) of premixed elemental powders. In 2021, Mitra et. al. employed a similar approach to fabricate titanium-tantalum alloys for biocompatibility studies. Knoll et. al. used laser additive manufacturing (LAM) of premixed hot-working tool steel and Ni-based maraging steel powders to produce piecewise graded alloys. Moorehead et. al. demonstrated a multi-hopper directed energy deposition (DED) system, combined with CALPHAD modeling, to generate arrays of compositionally graded high entropy alloys (HEAs) for alloy discovery. More recently, Vecchio et. al. reported an integrated high-throughput alloy development framework that combines


Distribution Statement A: Approved for public release. Distribution is unlimited.

computational screening, laser metal deposition (LMD), and a machine learning algorithm to establish compositional-property relationships. The importance of such relationships in graded materials has long been recognized; for example, Collins et. al. studied property-compositional correlations in graded titanium-vanadium and titanium-molybdenum alloys more than two decades ago.

### 1.3 Additive Manufacturing As-Built Microstructure

Additive manufacturing processing involves localized melting and solidification at fine length scales, which produces steep thermal gradients and exceptionally high cooling rates. Work by Heng reported cooling rates for DED on the order of 3000K/s with gradients of 483 K/mm along the melt pool width and 1416 K/mm along the depth. Cooling rates for laser welding have similarly been reported in the $10^3 – 10^5$ K/s range, and upward of $10^6$ K/s in laser powder bed fusion (L-PBF). These solidification conditions give rise to a distinctive as-built microstructure. The initial deposition layer partially remelts the substrate (often wrought or cast plate), leading to epitaxial grain growth from the fine equiaxed base material into the fusion zone. Subsequent layers experience steep thermal gradients along the build direction, promoting competitive grain growth that quickly selects favorably orientated grains. In thin-walled geometries, this process typically produces a fine <100> texture in cubic materials aligned with the steepest thermal gradient (parallel to the build direction). With continued deposition, these favorably orientated grains continue growing epitaxially to form a coarser columnar structure, a morphology that has been reported in nickel-based superalloys , for prior-β gains in Ti-6Al-4V, and stainless steels.

Recent work has demonstrated that melt-scan strategies can be used to exploit the relationship between solidification parameters and grain orientation selection. Through a combination of numerical modeling and experimental validation, researchers have shown that tailoring the thermal gradient to solidification ratio (G/R) enables local control of as-built grain structure including morphology, size, and primary dendrite arm spacing , as well as crystallographic texture for IN718 using electron beam AM. Similarly, using a scan strategy-based method, Kumar et. al. achieved comparable results in 316L stainless steel. However, the effectiveness of the scan strategies approach is largely constrained to multi-pass, multi-layer builds where controlling cooling within the build plane (XY) and along the build direction (Z) are possible. In contrast, thin-walled single-pass builds—such as in the present work—offer less control over thermal management. Consequently, the specimens analyzed here developed both compositional and microstructural gradients along the build direction, a combination that directly and simultaneously impacts their tribocorrosion performance.

## 2. Experimental Procedure

### 2.1 Materials

The alloys of interest in the present study are austenitic 316L stainless steel (UNS S31603) and super austenitic stainless steel AL6XN (UNS N08367). Using average compositions across their allowable specification range as wrought alloys, 316L stainless steel exhibits a pitting resistance


Distribution Statement A: Approved for public release. Distribution is unlimited.

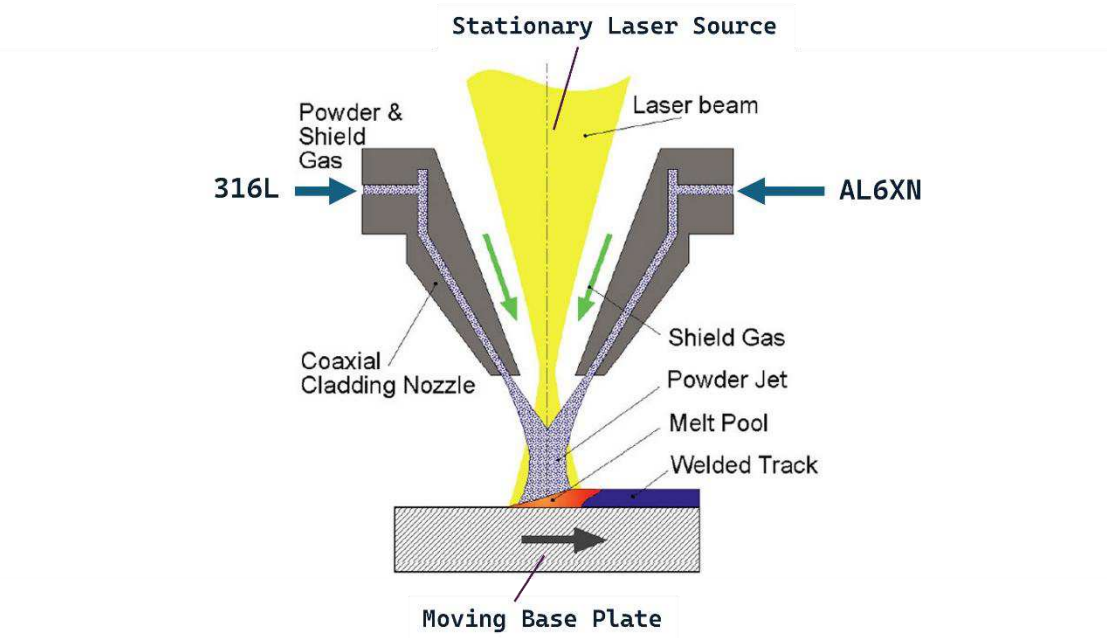
equivalent number (PREN) of approximately 26, and AL6XN has an average PREN of 46. The measured chemical compositions of the baseplate material and both powders are summarized in Table 1. Notably, the 316L powder exhibited a higher than anticipated PREN value of 30.6, attributed to an elevated nitrogen concentration. This is likely a result of nitrogen gas entrapment during the powder production process, a known phenomenon in gas-atomized powders.

Table 1. Composition and associate PREN for the 316L and AL6XN powders, and the wrought AL6XN baseplate.

| | Ni | Cr | Mo | N | PREN |
|---|---|---|---|---|---|
| **316L powder** | 11.00 | 17.00 | 2.00 | 0.44 | 30.6 |
| **AL6XN powder** | 25.34 | 20.52 | 6.32 | 0.21 | 44.7 |
| **AL6XN baseplate** | 23.68 | 20.75 | 6.14 | 0.22 | 44.5 |

2.1.1 Compositionally Varied Sample Fabrication via DED

A Hurco/Hybrid directed energy deposition (DED) system was employed to fabricate a single-pass, multi-layer, thin-wall structure by laser melting blown alloy powders onto a wrought AL6XN baseplate. The system utilizes a 1000W Nd:YAG laser power source with a 300 mm/min scan speed to achieve the requisite fusion of the alloy powders. To create the compositional gradient, a two-feed hopper system (illustrated in Figure 1) was implemented, allowing for precise control of the powder volume ratios between 316L stainless steel and AL6XN during each successive melting pass. The resulting build featured a height of approximately 20 mm and a width of 3 mm. Following deposition, individual samples, including the wrought baseplate, were sectioned using a wire electrical discharge machine (EDM). This methodology enables controlled integration and spatial control, thus facilitating compositional gradients along the build direction, and permitting tribocorrosion experimentation across the gradient.





Distribution Statement A: Approved for public release. Distribution is unlimited.

Figure 1. Schematic of the dual-hopper directed energy deposition (DED) additive manufacturing system used to fabricate thin-walled, compositionally graded stainless steel samples.

### 2.1.2 Tribocorrosion Sample Preparation

Sectioned samples were grouped in sets of three and mounted in a non-conductive epoxy. An insulated copper wire was soldered to each sample prior to mounting to establish a reliable electrical connection necessary for electrochemical testing. Following mounting, all samples underwent mechanical polishing to a 1 μm suspended diamond finish. To eliminate any residual debris or polishing media, all samples were ultrasonically cleaned in deionized water and subsequently rinsed with ethanol. Cleaned samples were dried under a stream of nitrogen gas and stored in a desiccator containing a drying agent for a minimum of 24 hours prior to testing.

To control and standardize the active surface area, non-conductive electroplaters tape was adhered to the target specimen creating an exposure window of approximately 38 $mm^2$. This includes covering adjacent samples in the mounted triplet to prevent any unintended electrochemical interactions and to preserve any pre-existing wear tracks from previous tests. Attention was given to prevent potential wetting under the tape seams at the periphery of the exposure window as this could form a crevice-like environment which may act to significantly accelerate localized corrosion beyond the rates expected within the wear track itself. Additionally, the exposure window was positioned to avoid the sample-epoxy interface, which is similarly susceptible to crevice corrosion initiation if exposed to the electrolyte.

## 2.2 Linear Reciprocating Tribocorrosion Experimentation

Tribocorrosion experiments were conducted using a custom-designed reciprocating linear tribometer detailed elsewhere. The tribometer, illustrated in Figure 2, consists of an insulated polyvinyl chloride (PVC) electrochemical cell with polymer grips to fix the sample in place. A three-electrode configuration was used to enable reliable in-situ electrochemical responses during mechanical wear. A platinum mesh along the interior periphery was the counter electrode, and a saturated calomel reference electrode (SCE) served as the reference electrode. The reference electrode was placed in close proximity to the exposed stainless steel sample window (working electrode) to minimize solution resistance.


Distribution Statement A: Approved for public release. Distribution is unlimited.

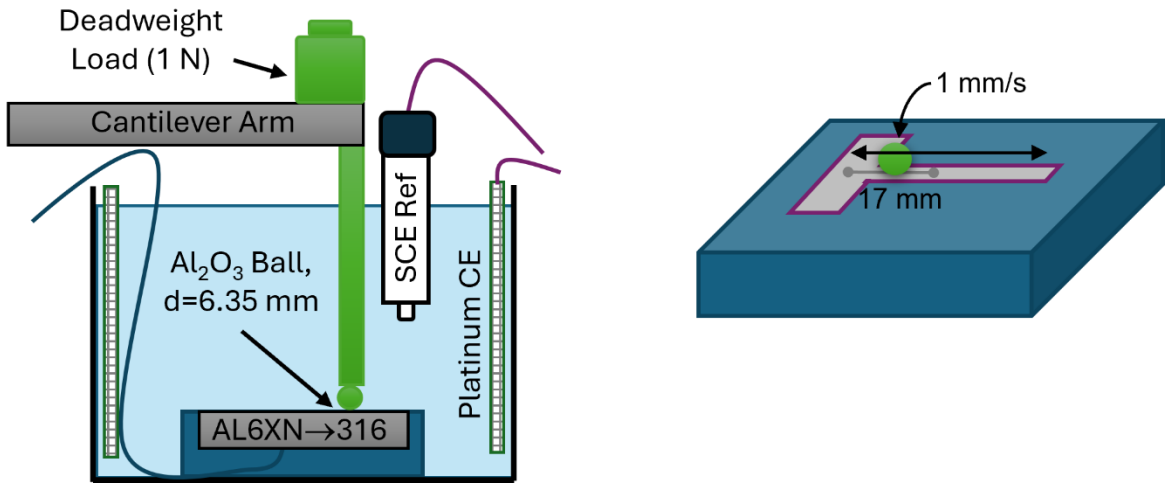



Figure 2. Left: schematic of custom tribocorrosion test cell; right: illustration of counterbody sliding pattern along the build direction of AM samples.

A 1 N normal load was applied to a 6.35 mm diameter alumina ball serving as the reciprocating counterbody as shown in Figure 13. Alumina has negligible plastic deformation during sliding experiments and is not susceptible to corrosion or galvanic coupling with the test material. The maximum and average Hertzian contact stresses were calculated using the classical solution for non-adhesive elastic contact between a rigid sphere and elastic half-space and were 0.73 GPa and 0.49 GPa respectively. These applied stresses are sufficient to locally disrupt the passive oxide film and induce plastic deformation of the metal surface but were not expected to exceed the ultimate tensile strengths of the alloys of interest. Sliding amplitude was 17 mm, orientated parallel to the build direction, and was limited to just the AM region of the specimen. A constant sliding speed of 1 mm/s was maintained throughout sliding, and each experiment consisted of 100 total cycles.

The present study was only focused on anodic potentials within the passive regime for both alloys to investigate the electrochemical behavior of the alloys under tribocorrosion conditions. Fixed potentials of +100 $mV_{SCE}$, +200 $mV_{SCE}$, and +300 $mV_{SCE}$ were used in this study with a 0.6 M NaCl solution serving as the electrolyte. Prior to sliding, each sample was held at the target potential for a conditioning period of 30 minutes to ensure the metal surface has reached a stable electrochemical equilibrium and to quantify the baseline current prior to sliding.

## 2.3 Characterization and Data Analysis

Current was measured using a Gamry Reference 600 potentiostat, and the coefficient of friction was determined from strain gauges mounted on the load arm. The volume of oxidized material ($V_a$) generated during sliding was calculated using Faraday's Law, as expressed by Eq. (1). In this relation, $Q_{Sliding}$ represents the charge exchange due to tribocorrosion processes, which was obtained by integrating the measured current during sliding after subtracting the baseline current. $M$ denotes the alloy molecular weight, $n$ is the number of electrons involved in the electrochemical reaction, $F$ is Faraday's Constant, and $\rho$ is the alloy density. The values of $M$, $n$, and $\rho$ used in this study, together with the chemical compositions used to calculate $n$, are provided in Table 2. It is


Distribution Statement A: Approved for public release. Distribution is unlimited.

important to note that these parameters are dependent upon the local alloy composition, which, across much of the build domain, consists of a heterogeneous mixture of 316L and AL6XN stainless steels. As a result, the actual values of $M$, $n$, and $\rho$ are non-constant.

$$V_a = \frac{Q_{Sliding} \cdot M}{n \cdot F \cdot \rho} \tag{1}$$

Accounting for such spatial variation would require significant additional assumptions and complexity. Therefore, in the present work, $V_a$ was calculated twice: once using material constants corresponding to 316L and again using those for AL6XN. The true values are expected to lie between these two bounds, with the oxidation behavior better approximated by the 316L-based calculation near the top of the build and by the AL6XN-based calculation closer to the base plate.

Table 2. Chemical compositions of AM powders and the corresponding molecular weight, density, and number of electrons involved in the electrochemical reaction.

| | Fe | Cr | Mo | Ni | $M\ (g/mol)$ | $\rho\ (g/cm^3)$ | $n$ |
|---|---|---|---|---|---|---|---|
| 316L | 66 | 17 | 2.5 | 12 | 55.6 | 7.99 | 2.17 |
| AL6XN | 45 | 21 | 6.5 | 24.5 | 56.6 | 8.06 | 2.26 |

In tribocorrosion experimentation, the overall wear rate is generally calculated by normalizing the total volume of material lost ($V_{Tot}$) along the entire wear track by the applied normal force ($F_N$) and total travel length of the counterbody during sliding ($L$) as expressed by Eq. (2). This formulation is mathematically equivalent to the ratio of the product of an average wear track cross sectional area ($A_{Avg}$) and the stroke length of the counterbody ($l_{Stroke}$) to the applied normal force multiplied by twice the stroke length (to account for both the forward and reverse sliding) and the total number of cycles ($N_{Cycles}$). For the present work, it is advantageous to calculate wear rates at discrete points along the build as wear rate is dependent upon the local wear and corrosion resistance, which are expected to vary along the compositional and microstructural gradient of the AM specimens. By considering the cross-sectional area of the wear track at a discrete point rather than as a global average, Eq. (2) can be reformulated as Eq. (3) which therefore calculates the expected wear rate based on conditions at a given location. This approach facilitates direct comparisons of wear rates along the AM samples.

$$Average\ Wear\ Rate = \frac{V_{Tot}}{F_N L} = \frac{A_{Avg} \cdot l_{Stroke}}{F_N \cdot 2 l_{Stroke} \cdot N_{Cycles}} \tag{2}$$

$$Discrete\ Wear\ Rate = \frac{A \cdot l_{Stroke}}{F_N \cdot 2 l_{Stroke} \cdot N_{Cycles}} \tag{3}$$


Distribution Statement A: Approved for public release. Distribution is unlimited.

# 3. Results

## 3.1 Thin-walled DED Sample As-Built Microstructure

An untested sample was polished for electron microscopy and examined using an FEI environmental scanning electron microscope (SEM). Backscattered electron imaging (Figure 3, left) reveals a fine, equiaxed grain structure in the AL6XN substrate, with a distinct fusion zone where remelting occurred during deposition of the first layer. At the base of the build, epitaxial grains are observed to grow along the thermal gradient—both inward toward the build center and upward in the build direction. The grains grow epitaxially through multiple layers, producing a microstructure in which individual build layers blend together. Toward the top of the build, where the composition is fully 316L, the microstructure has fully evolved into a highly columnar morphology consisting of only a few large grains.

The same regions were further characterized by electron backscatter diffraction (EBSD), as shown on the right side of Figure 3. EBSD analysis, which provides crystallographic orientation mapping, confirms the presence of distinct austenitic grains and reveals the development of a preferential <100> texture typical of face-centered cubic additively manufactured alloys as shown in Figure 14. While a more thorough texture analysis lies outside the scope of this work, the primary limitation to the strength of the formed texture was attributed to the limited grain population after the first few melting passes due to the thin-walled structure. In contrast, conventional AM components fabricated with multiple overlapping passes experience re-melting both parallel and perpendicular to the build direction, thereby increasing the available remelt volume from which preferentially orientated grains can grow thus enhancing the strength of the crystallographic texture.


Distribution Statement A: Approved for public release. Distribution is unlimited.

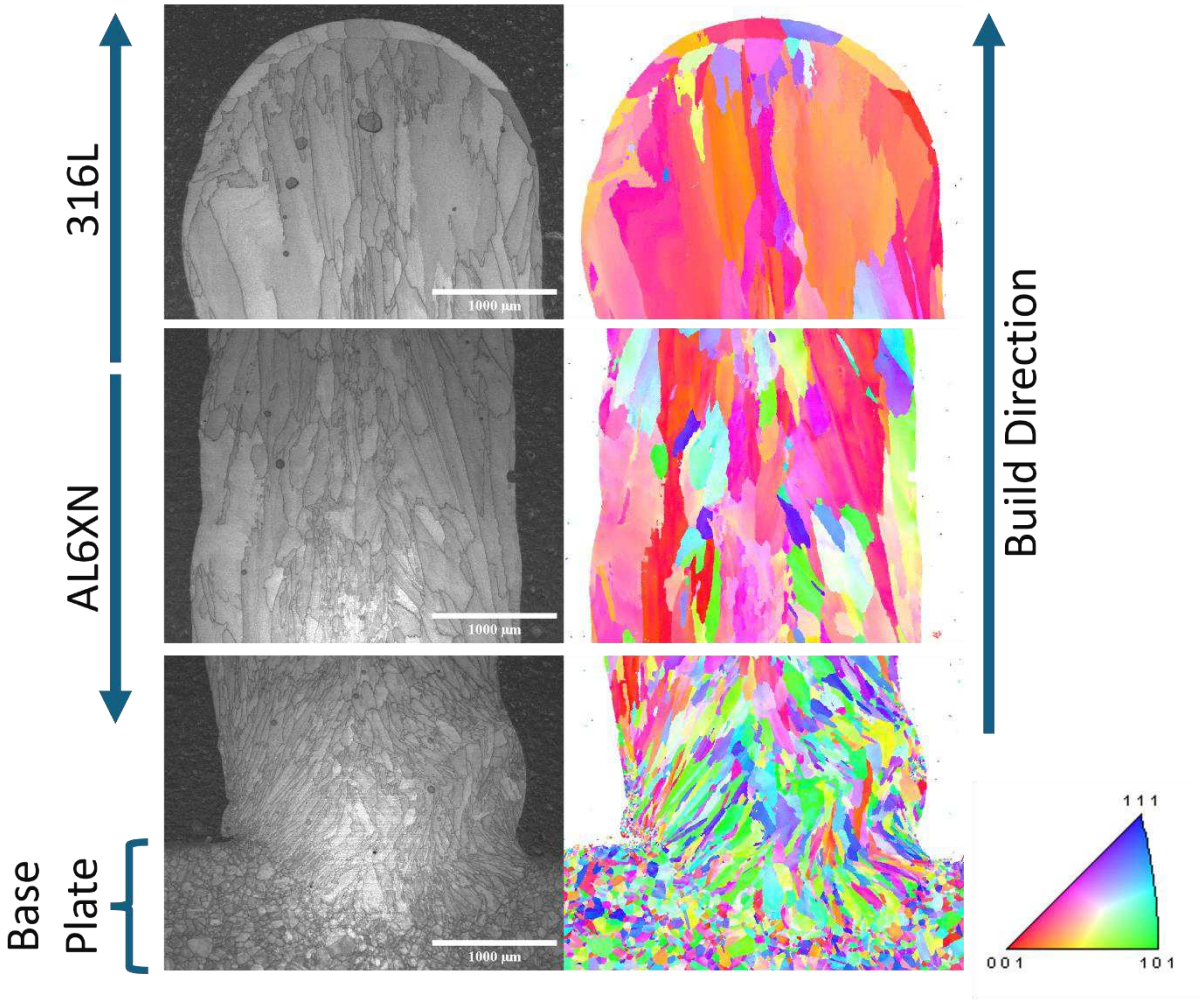



Figure 3. Inverse pole figure mapping of the as-built, thin-wall additive manufacturing grain structure scanned using EBSD. Fine grain structure of wrought AL6XN baseplate quickly transitions into large epitaxially grown columnar grains due to growth competition following the temperature gradient.

3.2 Hardness Gradient

To quantify this microstructural influence, microhardness testing was performed along the build height. The results, shown in Figure 4, confirmed a trending decrease in hardness from approximately 250 HV near the baseplate to 180 HV at the top of the build. This trend is consistent with EBSD observations. Grain structure refinement at the base enhances hardness, and coarsening near the top reduces resistance to plastic deformation. These results suggest that the increasing wear rate along the build height (discussed in section 3.5) can be attributed, at least in part, to the reduced hardness and diminished wear resistance associated with the coarser microstructure.


Distribution Statement A: Approved for public release. Distribution is unlimited.




Figure 4. Hardness measurements show a gradual decrease along the height of the build as grain growth competition gradually coarsens the as-built grain structure.

### 3.3 Compositional Gradient

Composition along the build direction was measured and used to calculate the pitting resistance equivalent number (PREN) at discrete locations using energy-dispersive spectroscopy (EDS), which confirmed the successful fabrication of a compositionally graded AM build. At each measurement location, three individual point scans across the sample width were acquired and averaged. Measurements were performed approximately every 850 µm from the baseplate upward. Results from three independently analyzed samples are presented in Figure 5 and reveal a continuous transition from the higher PREN of AL6XN (~42) near the baseplate to the lower PREN of 316L (~25) toward the top of the build. PREN values were calculated without accounting for nitrogen as its concentration was too low to be reliably detected by EDS. Consequently, the absolute PREN values may be slightly underestimated; however, this limitation does not affect the observed compositional trend. Although more precise compositional analysis methods are available, the EDS measurements provide sufficient resolution to confirm the presence of a gradual chemical compositional gradient with the samples.


Distribution Statement A: Approved for public release. Distribution is unlimited.

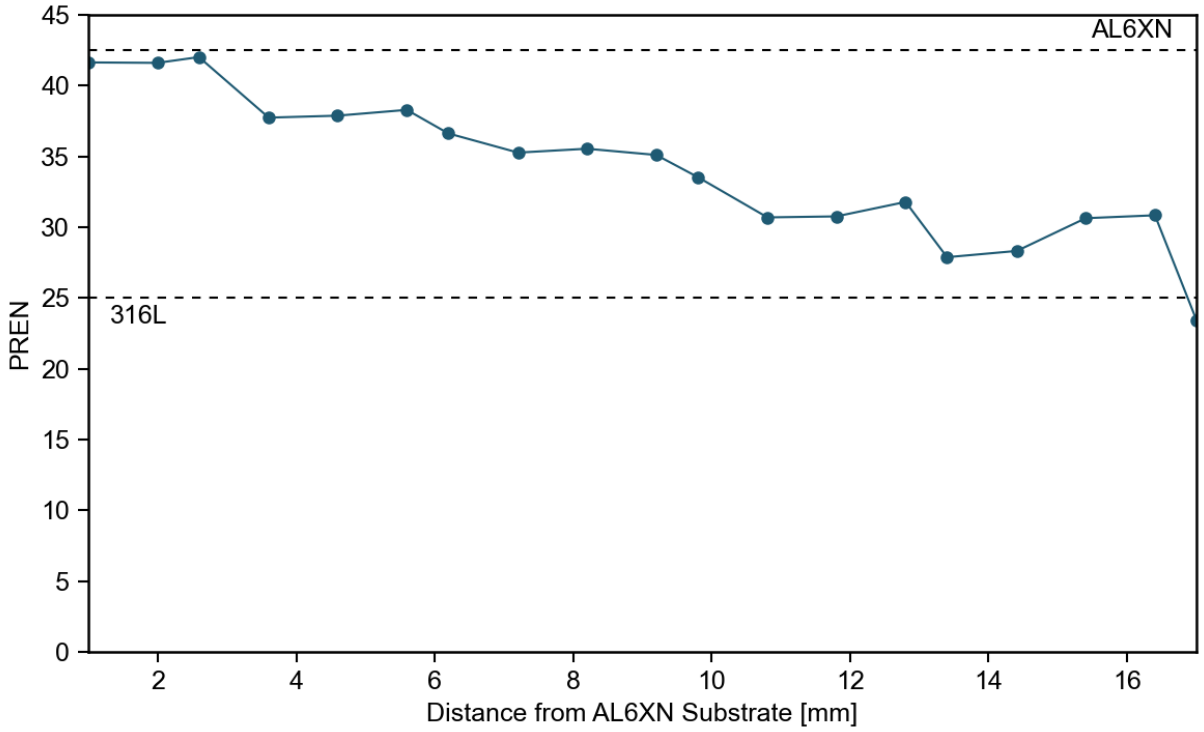



Figure 5. Pitting resistance equivalent number (PREN) along the build direction calculated using EDS chemical composition measurements along the full length of the build.

3.4 Wear-Enhanced Corrosion Electrochemical Response

During each tribocorrosion experiment the current was recorded for 300 seconds prior to sliding and for 300 seconds after sliding ceased to establish the baseline dissolution current of the undisturbed passive surface. Each sample was tested under three anodic applied potentials within the passive regime of the alloys, ensuring that the active surface could re-passivate in the wake of the counterbody at all conditions. Representative current measurements for sample 6 at all three potentials, including the pre- and post-sliding baseline holds, are shown in Figure 6. Upon initial contact between the counterbody and the sample, the current rose sharply indicating an increase in electrochemical reaction rate due to a local disruption of passivity. During the first few sliding cycles, the current remained relatively low while the counterbody ruptured the oxide layer and exposed small areas of the underlying metal. With continued sliding, the current increased progressively as successive passes opened larger regions of exposed surface. A local current peak was observed spanning several cycles, corresponding to the point where the rates of mechanical de-passivation and electrochemical re-passivation equilibrated, while the active surface area was maximized due to asperity disruption. This was followed by a moderate decrease to a stable steady-state current as the wear track evolved—characterized by asperity flattening or smearing and surface smoothing as demonstrated by Mischler and colleagues. Average current remained relatively constant until sliding was halted, after which it rapidly returned near to the low baseline value observed prior to sliding, indicating complete re-passivation of the exposed surface. This behavior confirms that the elevated current during sliding arose from repetitive rupture-


Distribution Statement A: Approved for public release. Distribution is unlimited.

repassivation cycling. Moreover, the lack of a sustained increase in current during or following sliding demonstrates that sustained pitting or other localized corrosion processes were not initiated under the applied conditions.

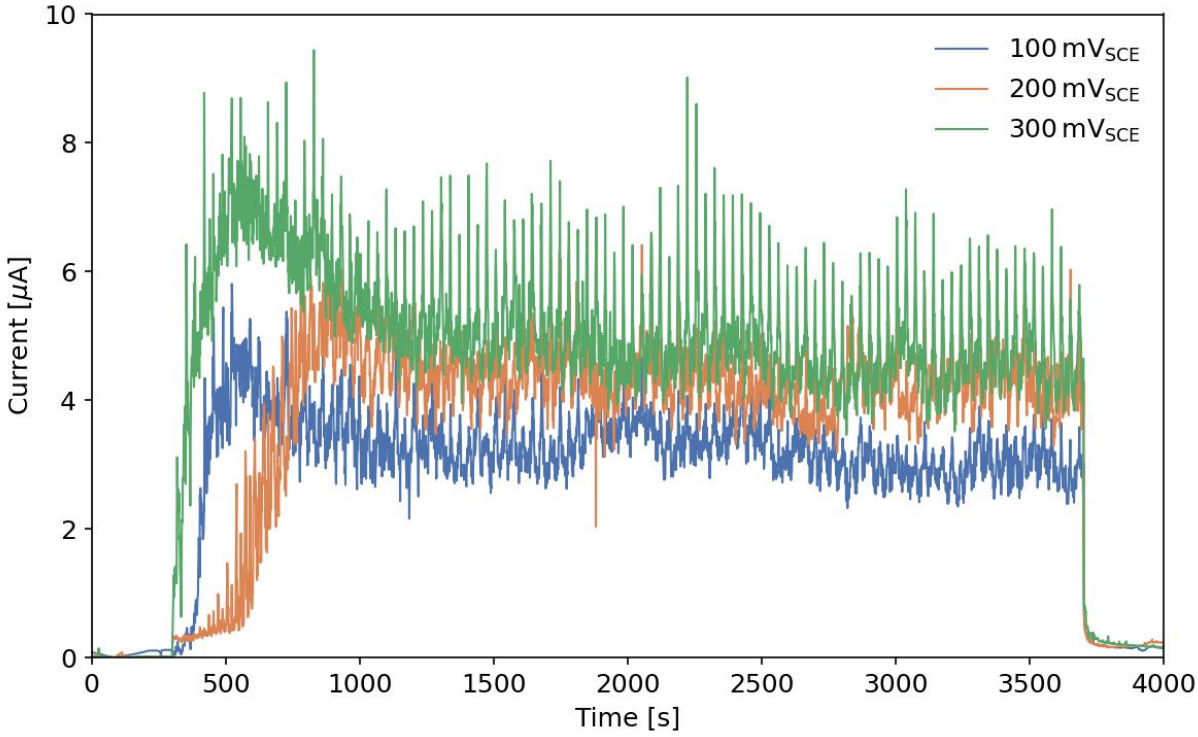



Figure 6. Current measurements during sliding at 100, 200, and 300 $mV_{SCE}$ showing an increase in average current with applied potential.

One notable feature in Figure 6 is the presence of repeated, cyclical peaks and valleys in the current measurements during sliding, indicating oscillatory behavior in the electrochemical reaction rate. This effect is most pronounced at the 300$mV_{SCE}$ applied potential. By isolating a single valley-to-peak fluctuation and comparing the measured data with tabulated counterbody position (Figure 7), it was determined that valleys occur when the counterbody is located at the base of the build on the AL6XN side, whereas peaks arise on the 316L side at the top of the build. These observations are consistent with the initial hypothesis: the more corrosion resistant AL6XN likely repassivates more rapidly, leaving less exposed bare metal surface at any given time compared to the less corrosion resistant 316L. Although still within the passive regime, the highest applied potential (300 $mV_{SCE}$) approaches the breakdown potential of the 316L passive film in 0.6 M NaCl and may be sufficiently high to promote metastable pit initiation, which likely produces the pronounced differences in current response between the 316L and AL6XN regions of the additively manufactured build.


Distribution Statement A: Approved for public release. Distribution is unlimited.

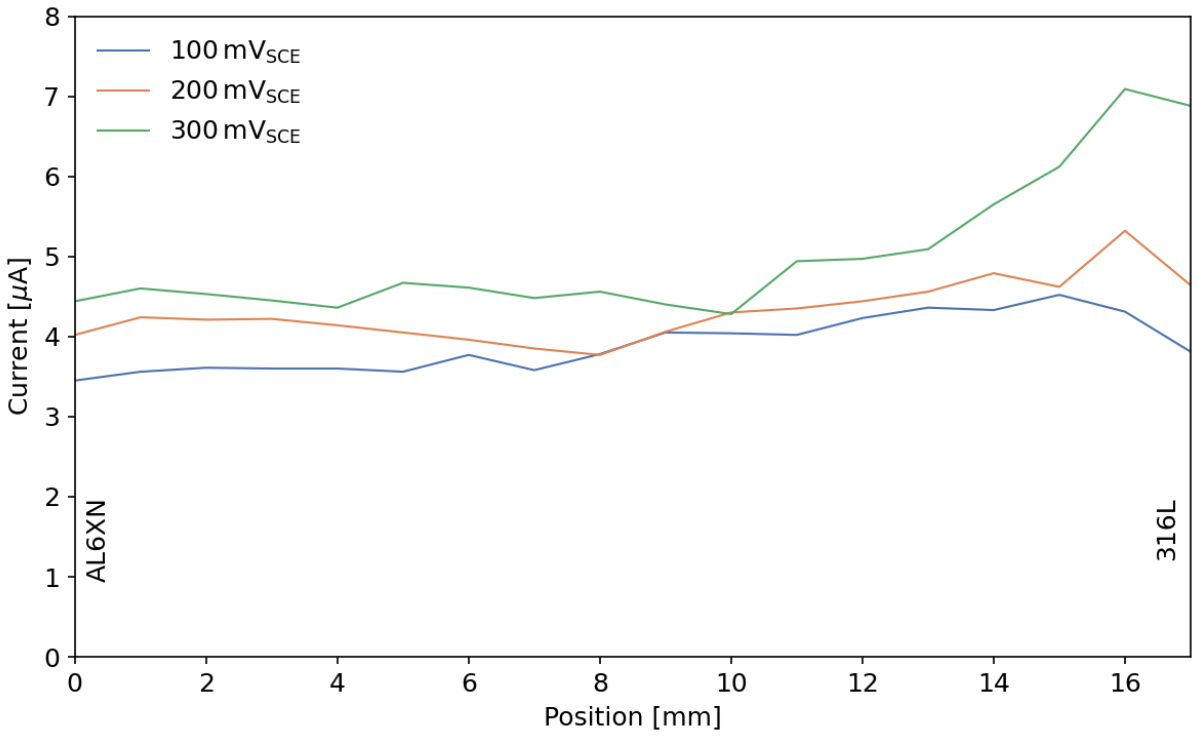
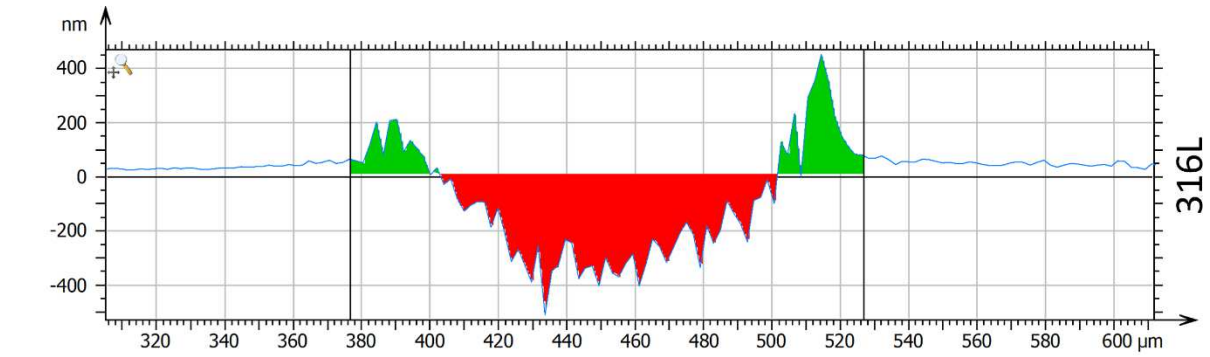



Figure 7. Current measurements as a function of counterbody position along the wear track during a single half-cycle showing an elevation in measured current while sliding across the 316L end of the build.

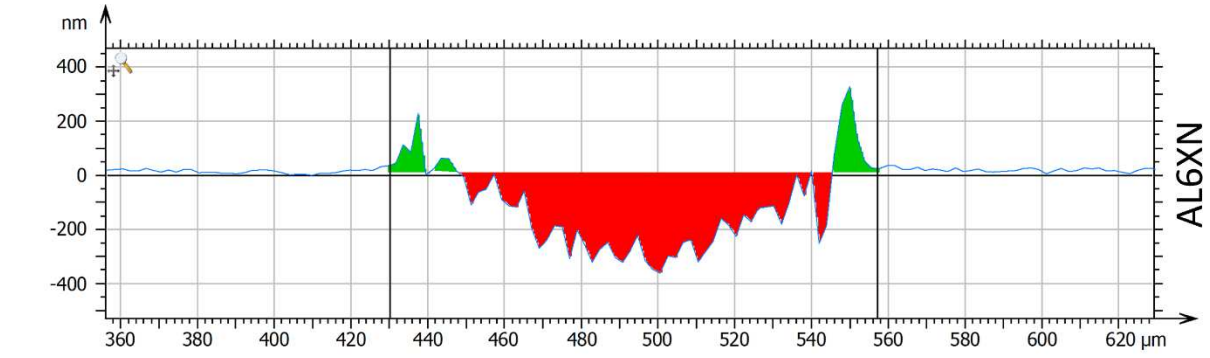
3.5 Wear Rate and Coefficient of Friction

White light interferometry was employed to characterize the wear tracks produced during tribocorrosion testing. Representative two-dimensional cross-sectional profiles obtained from each end of the wear track for Sample 8 after testing at an applied potential of 100 mV$_{SCE}$ are presented in Figure 8. After 100 linear reciprocating cycles, the cross sections reveal wear tracks on the 316L side of the build that were up to 40% deeper than those on the AL6XN side. In addition to greater penetration depth, the 316L region exhibited substantially more pronounced ploughing behavior with material pileup along the periphery of the wear track, accompanied by deeper grooves. Differences between the two alloys remained pronounced at 200 and 300mV$_{SCE}$ applied potentials.


Distribution Statement A: Approved for public release. Distribution is unlimited.




| Parameters | Value | Unit |
|---|---|---|
| Maximum depth | 528 | nm |
| Area of the hole | 24722635 | nm² |
| Maximum height | 434 | nm |
| Area of the peak | 6832892 | nm² |




| Parameters | Value | Unit |
|---|---|---|
| Maximum depth | 380 | nm |
| Area of the hole | 20372612 | nm² |
| Maximum height | 308 | nm |
| Area of the peak | 2499606 | nm² |

Figure 8. Cross-sectional area measurement of the wear track used in calculating discrete wear rates using Eq. (3).

To further examine the extent and morphology of wear, interferometric scans were stitched together to generate full-length wear track profiles, as shown in the center of Figure 9. The same trends observed in the cross-sectional profiles were evident in the three-dimensional topographical reconstructions. On the 316L side of the build (Figure 9, bottom), extensive material pileup and wide, deep wear grooves were observed. In contrast, the AL6XN side (Figure 9, top) displayed a markedly smoother surface with less severe topographical disruption, consistent with the superior tribocorrosion resistance of this portion of the sample. Importantly, the degradation evolved gradually along the compositional and microstructural gradient of the build, with no sharp transitions or piecewise changes in performance. This continuous evolution parallels the smooth chemical composition and hardness gradient measured along the build direction, further confirming the reproducibility and effectiveness of the graded structure.


Distribution Statement A: Approved for public release. Distribution is unlimited.

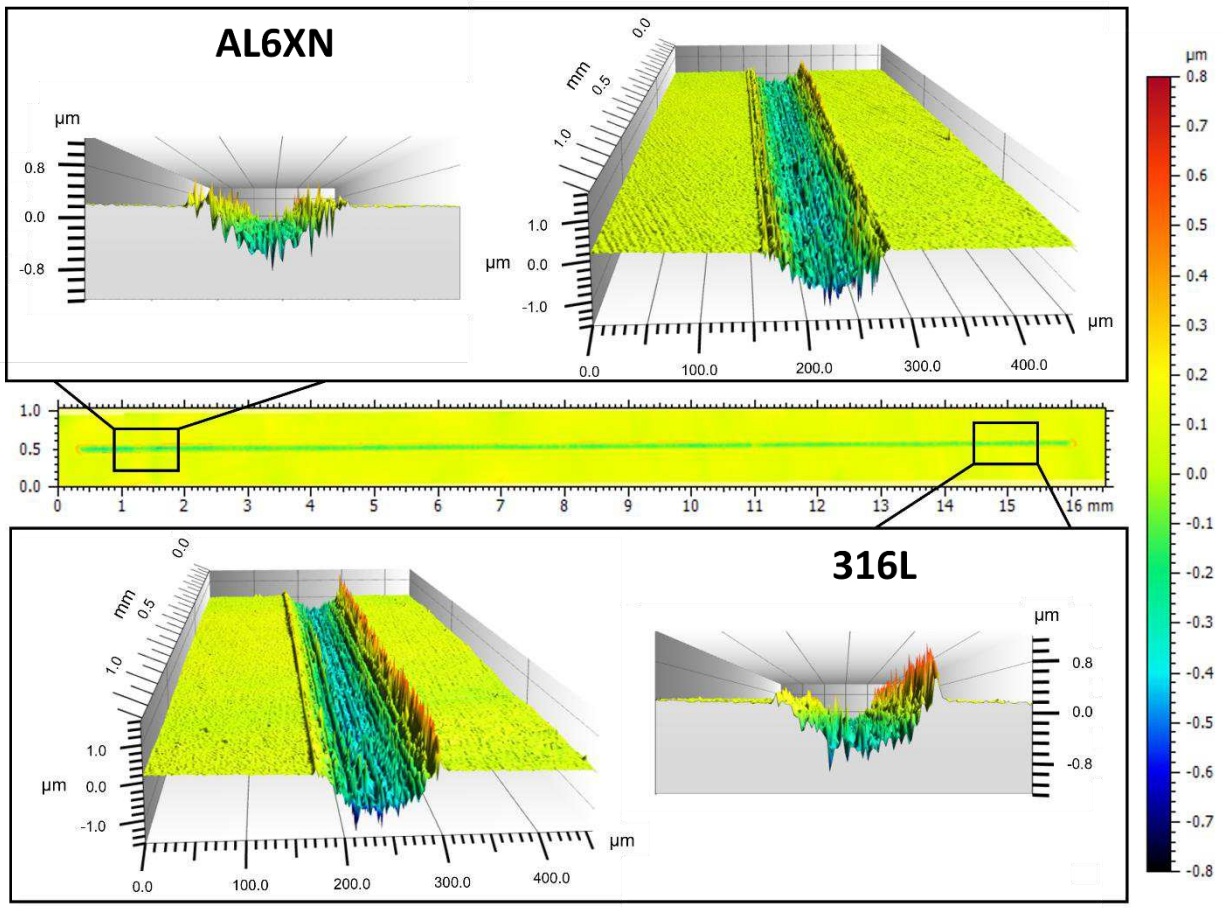



Figure 9. Wear track after 100 sliding cycles at 300 $mV_{SCE}$ applied potential in 0.6 M NaCl solution measured using white light interferometry. A deeper wear track is observed on the 316L end of the build with more prominent ploughing tracks at wear track periphery.

Wear tracks were analyzed using MountainsMap® software to determine cross-sectional area at discrete points along the track and calculate localized wear rates according to Eq. (3). By repeating this analysis at regular intervals of 0.5 mm along the build direction, a spatially resolved distribution of wear rate could be constructed, which enables visualization of how tribocorrosion behavior evolves continuously across the compositional gradient. The resulting mean wear rate profiles for all samples at applied potentials of 100 $mV_{SCE}$ and 300 $mV_{SCE}$ are shown in Figure 10. For both potentials, the calculated wear rate increased approximately linearly with distance from the AL6XN substrate, consistent with the compositional and hardness gradients discussed previously. The higher applied potential (300 $mV_{SCE}$) produced substantially greater wear rates overall, reflecting the impact of enhanced electrochemical activity on tribocorrosion behavior. Importantly, the trend of increasing wear rate with distance mirrors the inverse relationship with PREN and hardness as a function of position (Figures 4 and 5), further underscoring the link between composition, microstructure, and tribocorrosion performance.


Distribution Statement A: Approved for public release. Distribution is unlimited.

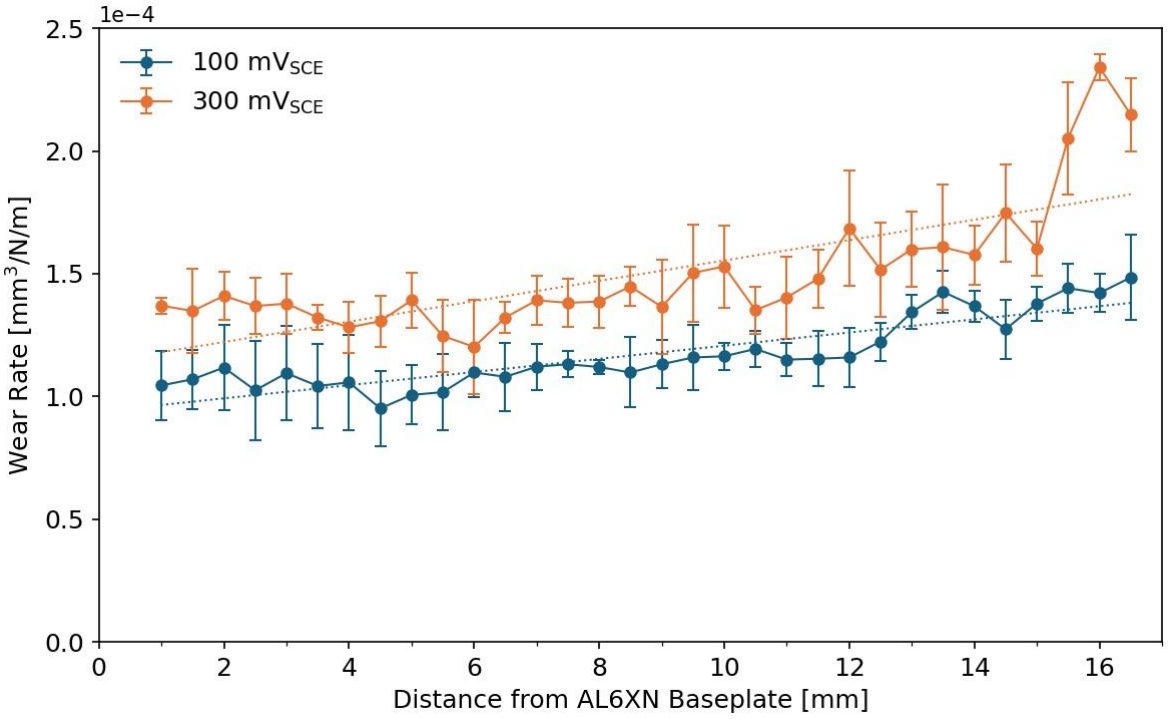



Figure 10. Calculated mean wear rate for all samples using Eq. (3) showing an increasing wear rate along the build direction with high wear rates on the 316L end of the build.

The coefficient of friction (COF) was continuously monitored during each sliding experiment. Data was acquired at a sampling interval of 0.125 s. The sign of the raw COF values depended on sliding direction of the counterbody, so values were processed to report the average magnitude relative to the baseline. Representative friction curves for two different samples tested at three applied potentials are shown in Figure 11 alongside the simultaneously measured current responses.

The coefficient of friction traces were consistent across all applied potentials, indicating that frictional behavior was largely insensitive to the electrochemical conditions within the range investigated. For all cases, the average COF remained within a narrow band of approximately 0.4-0.5. A gradual upward trend was observed during sliding at all potentials. This gradual increase is likely due to a combination of progressive work hardening, oxide/debris accumulation in the wear track, and repeated rupture/repassivation of the passive film, all of which may increase interfacial shear resistance. While initial smoothing of the wear track may reduce roughness, this effect is outweighed by the evolving tribocorrosion mechanisms that promote higher COF over time. The similarity of the COF behavior across potentials suggests that, although applied potential significantly influences the corrosion-driven component of material degradation, its effect on the mechanical frictional response is comparatively minor under the present conditions where potentials are within the passive regime for the alloys of interest.


Distribution Statement A: Approved for public release. Distribution is unlimited.

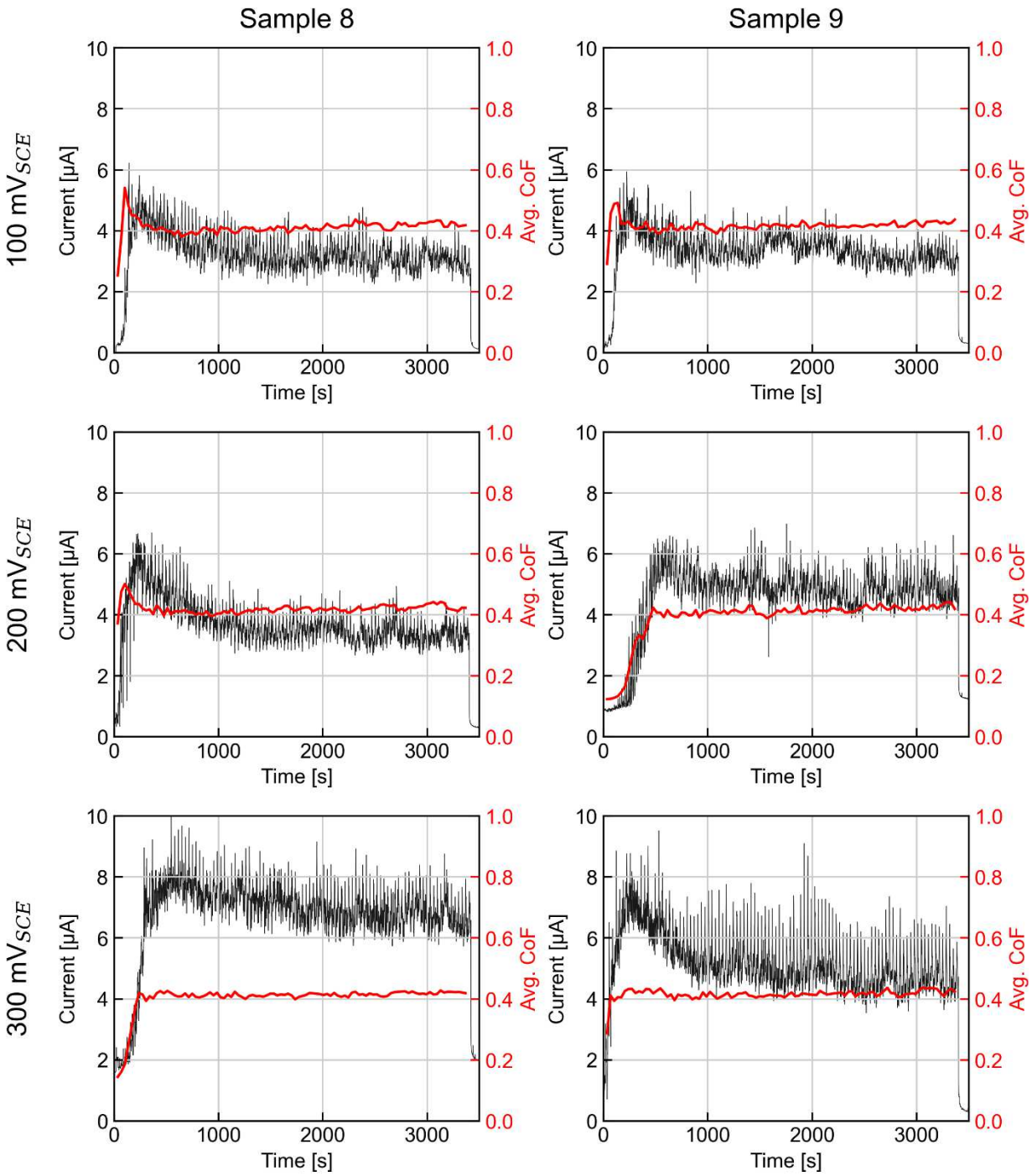



Figure 11. Current and average coefficient of friction (COF) plotted for two different samples as a function of time. Measured current profile shows a notable increase with applied potential, but coefficient of friction is relatively consistent for all conditions.


Distribution Statement A: Approved for public release. Distribution is unlimited.

3.5 SEM Wear Track Characterization

Electron microscopy of the wear tracks highlighted the disparity in surface degradation between AL6XN and 316L ends of the graded build. Figure 12 presents low- and medium-magnification backscattered electron (BSE) images of the wear track for sample 1 tested at an applied potential of 300 $mV_{SCE}$. On the AL6XN side of the specimen (top), surface damage was minimal and primarily limited to the mechanical wear scar imposed by the counterbody. Occasional dark regions were observed; however, subsequent inspection confirmed these features to be inherent porosity present throughout the build rather than corrosion products.

In contrast, the 316L end of the build (bottom) exhibited substantially more severe surface degradation. Numerous dark-contrast features, later confirmed by energy-dispersive spectroscopy (EDS) to be oxygen-enriched regions characteristic of localized corrosive attack, were observed on the 316L end of the build. These features are consistent with metastable pitting events that likely initiated during sliding under tribocorrosion conditions. The distribution of these dark spots gradually increases in density over the final 6-8 mm of the build as the composition transitioned fully to 316L. Conversely, the AL6XN end of the build showed minimal wear-enhance localized corrosion at the three potentials tested due to the higher Ni, Cr, and Mo content.

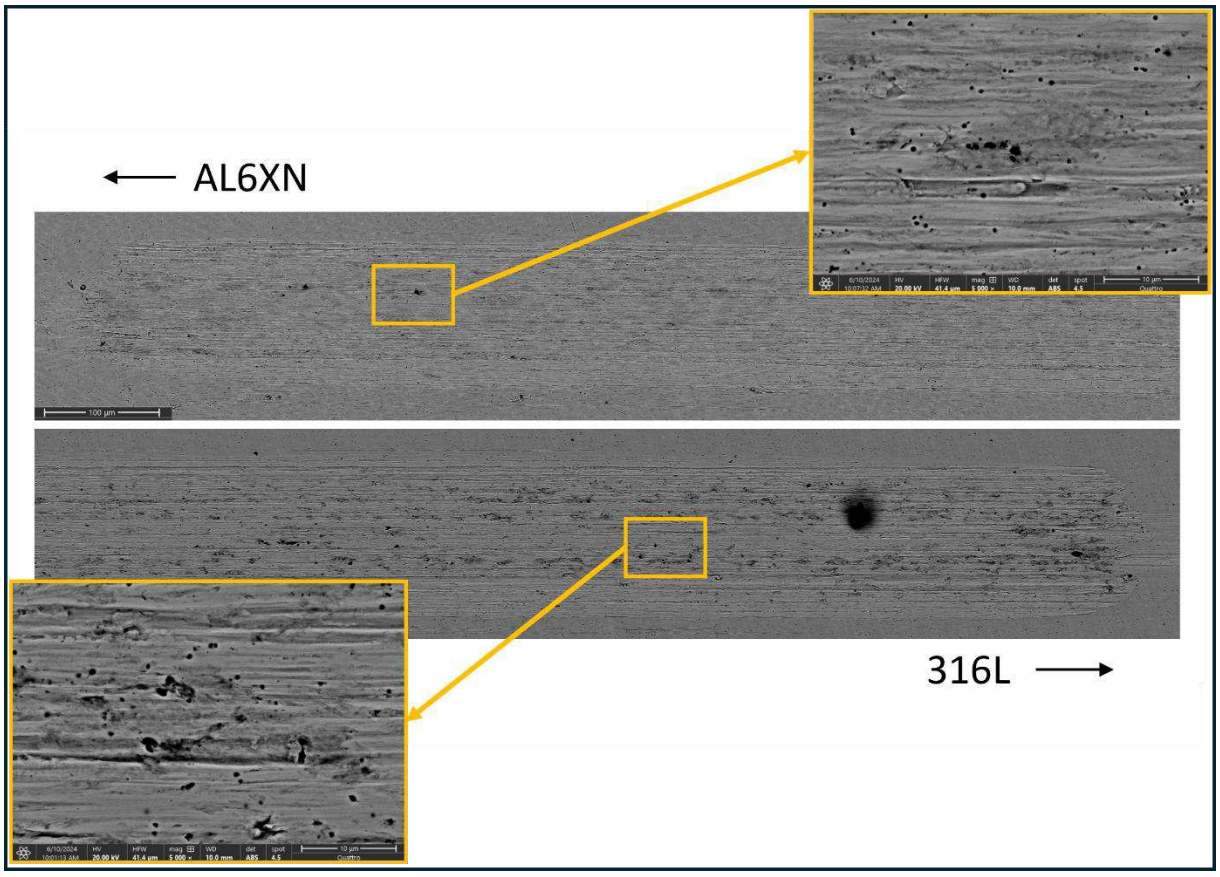



Figure 12. SEM backscatter imaging of the wear track showing significantly more surface degradation on the 316 end of the build.


Distribution Statement A: Approved for public release. Distribution is unlimited.

## 4. Discussion

### 4.1 Effect of AM Microstructure

Electron backscatter diffraction (EBSD) analysis revealed a pronounced evolution in the as-built microstructure of the thin-walled compositionally graded samples investigated in this work. The grain morphology varied significantly along the build direction, producing a corresponding gradient in mechanical properties. At the base of the build (Figure 3), the grain structure was considerably finer compared to the coarser grains observed toward the top. Such refinement at the bottom of the structure is expected to impede dislocation motion, thereby enhancing resistance to plastic deformation under contact with the hard alumina counterbody during tribocorrosion testing. Tribocorrosion performance is governed jointly by corrosion resistance and wear resistance, and changes in the underlying grain structure would be expected to modulate the mechanical response even in the absence of compositional variation.

### 4.2 Effect of Compositional Gradient

The additive manufacturing process employed in this study successfully produced thin-walled samples with a distinct compositional gradient. Energy-dispersive spectroscopy (EDS) confirmed this gradient, which translated directly into a variation in the pitting resistance equivalent number (Figure 5) and, by extension, corrosion resistance along the build height. While microstructural differences along the build direction influenced hardness and therefore wear resistance, as discussed previously, scanning electron microscopy (SEM) imaging (Figure 12) revealed a pronounced spatially dependent distribution of corrosion products after tribocorrosion testing. These results demonstrate that the microstructural gradient alone cannot account for the observed performance differences; rather, the combined effects of microstructure and composition governed the tribocorrosion response.

### 4.3 Additive Manufacturing as a Tool for Tribocorrosion Studies

Tribocorrosion is a complex synergy of wear and corrosion. The results presented here confirm that the tribocorrosion performance in the presently fabricated graded samples is governed by the interplay between mechanical resistance of the microstructure and electrochemical resistance of the local chemical composition, rather than by either mechanism in isolation. While a detailed mechanistic study of this synergy lies beyond the scope of the present work, these results underscore the unique value of additive manufacturing in tribocorrosion research. The ability to deliberately produce materials with both compositional and microstructural gradients provides a powerful platform for probing the coupled roles of wear and corrosion and offers a pathway toward more efficient screening of candidate materials and the rational design of alloys with improved resistance to wear-enhanced corrosion.

## 5. Conclusions

The present work demonstrates the value of additive manufacturing for producing compositionally graded samples as a platform for rapid alloy screening and development based on


Distribution Statement A: Approved for public release. Distribution is unlimited.

tribocorrosion performance. Using a two-hopper powder feed system, a continuous compositional gradient—and consequently a PREN gradient—from super-austenitic AL6XN stainless steel to austenitic 316L stainless steel was successfully fabricated and confirmed by energy dispersive spectroscopy. Electron backscatter diffraction revealed the characteristic microstructural evolution of thin-walled AM samples, beginning with fine elongated grains near the baseplate that follow the solidification thermal gradient, and transitioning into coarser columnar grains at higher build heights due to competitive grain growth under rapid solidification conditions.

Results revealed a clear inverse relationship between wear rate and the PREN gradient, consistent with the expected corrosion resistance differences between AL6XN and 316L. At the same time, wear rates also reflected the mechanical property gradient associated with the evolving microstructure, as confirmed by microhardness testing. Current transients measured during tribocorrosion experiments showed strong position dependence: higher currents in the 316L-rich region and lower currents in the AL6XN-rich region. SEM imaging confirmed the presence of corrosion products on the 316L side, suggesting (under the applied conditions) a compositional threshold beyond which surface degradation becomes significant.

This work highlights the interplay between microstructure-driven wear and composition-driven corrosion driving tribocorrosion performance of metal components. While quantifying the relative contributions of wear, corrosion, and their synergistic effects remains challenging, the present results demonstrate how compositionally, and microstructurally graded AM samples provide a useful approach to study these interactions. More broadly, this work demonstrates the potential of additive manufacturing in accelerating tribocorrosion research by enabling rapid screening of candidate alloys for material selection and supporting novel alloy development driven by wear-enhanced corrosion performance. Though outside the scope of this work, useful addition would be leveraging a creatively devised scan strategies for a 3D build in tandem with the demonstrated compositional grading process to isolate the compositional and microstructural variations and thereby permitting the investigation of each variable's individual influence on tribocorrosion performance.

## Acknowledgements

Funding for this work was provided by the Office of Naval Research through Dr. David A. Shifler, N0001421WX01787. The authors would also like to thank Dr. Kathryn Wahl for the counterbody surface imaging, Dr. John Steuben for the AM sample fabrication, and Dr. Derek Horton for the corrosion and profilometry analysis insight.

# References

[1] N. Diomidis, J. -P. Celis, P. Ponthiaux and F. Wenger, "tribocorrosion of stainless steel in sulfuric acid: Identification of corrosion-wear components and effect of contact area," *Wear,* vol. 269, pp. 93-103, 2010.



Distribution Statement A: Approved for public release. Distribution is unlimited.

[2] F. Assi and H. Böhni, "Study of wear-corrosion synergy with a new microelectrochemical technique," *Wear,* Vols. 233-235, pp. 505-514, 1999.

[3] S. W. Watson, F. J. Friedersdorf, B. W. Madsen and S. D. Cramer, "Methods of measuring wear-corrosion synergism," *Wear,* Vols. 181-183, pp. 476-484, 1995.

[4] S. Mischler, A. Spiegel and D. Landolt, "The role of passive oxide films on the degradation of steel in tribocorrosion systems," *Wear,* Vols. 225-229, pp. 1078-1087, 1999.

[5] S. Barril, S. Mischler and D. Landolt, "Triboelectrochemical investigation of the friction and wear behaviour of TiN coatings in a neutral solution," *Tribology International,* vol. 34, pp. 599-608, 2001.

[6] M. M. Stack and K. Chi, "Mapping sliding wear of steels in aqueous conditions," *Wear,* vol. 255, pp. 456-465, 2003.

[7] D. Landolt, S. Mischler, M. Stemp and S. Barril, "Third body effectsa nd material fluxes in tribocorrosion systems involving a sliding contact," *Wear,* vol. 256, pp. 517-524, 2004.

[8] J. Jiang, M. M. Stack and A. Neville, "Modelling the tribo-corrosion interaction in aqueous sliding conditions," *Tribology International,* vol. 35, pp. 669-679, 2002.

[9] S. Mischler, "Triboelectrochemical techniques and interpretation methods in tribocorrosion: A comparative evaluation," *Tribology International,* vol. 41, pp. 573-583, 2008.

[10] Y. Sun and V. Rana, "Tribocorrosion behaviour of AISI 304 stainless steel in 0.5M NaCl Solution," *Materials Chemistry and Physics,* vol. 129, pp. 138-147, 2011.

[11] P. Ponthiaux, F. Wenger, D. Drees and J. P. Celis, "Electrochemical techniques for studying tribocorrosion processes," *Wear,* vol. 256, pp. 459-468, 2004.

[12] J. M. Shockley, D. J. Horton and K. J. Wahl, "Effect of aging of 2507 super duplex stainless steel on sliding tribocorrosion in chloride solution," *Wear,* Vols. 380-381, pp. 251-259, 2017.

[13] P. Jemmely, S. Mischler and D. Landolt, "Tribocorrosion behaviour of Fe-17Cr stainless steel in acid and alkaline solutions," *Tribology International,* vol. 32, pp. 295-303, 1999.

[14] P. Henry, J. Takadoum and P. Berçot, "Tribocorrosion of 316L stainless steel and TA6V4 alloy in H2SO4 media," *Corrosion Science,* vol. 51, pp. 1308-1314, 2009.

[15] R. K. W. Marceau, C. Qiu, S. P. Ringer and C. R. Hutchinson, "A study of the composition dependence of the rapid hardening phenomenon in Al-Cu-Mg alloys using diffusion couples," *Materials Science and Engineering A,* vol. 546, pp. 153-161, 2012.

[16] D. C. Hofmann, J. Kolodziejska, S. Roberts, R. Otis, R. P. Dillon, J. Suh, Z. Liu and J. P. Borgonia, "Compositionally graded metals: A new frontier of additive manufacturing," *Materials Research Society,* vol. 29, no. 17, 2014.


Distribution Statement A: Approved for public release. Distribution is unlimited.

[17] M. Fischer, D. Joguet, G. Robin and P. Laheurte, "In situ elaboration of a binary Ti-26Nb alloy by selective laser melting of elemental titanium and niobium mixed powders," *Materials Science and Engineering C,* vol. 62, pp. 852-859, 2016.

[18] I. Mitra, S. Bose, W. S. Dernell, N. Dasgupta, C. Eckstrand, J. Herrick, M. J. Yaszemski, S. B. Goodman and A. Bandyopadhyay, "3D Printing in alloy design to improve biocompatibility in metallic implants," *Materials Today,* vol. 45, pp. 20-34, 2021.

[19] H. Knoll, S. Ocylok, A. Weisheit, H. Springer, E. Jagle and D. Raabe, "Combinatorial Alloy Design by Laser Additive Manufacturing," *Steel Research International,* vol. 88, no. 8, p. 1600416, 2017.

[20] M. Moorehead, K. Bertsch, M. Niezgoda, C. Parkin, M. Elbakhshwan, K. Sridharan, C. Zhang, D. Thoma and A. Couet, "High-throughput synthesis of Mo-Nb-Ta-W high-entropy alloys via additive manufacturing," *Materials and Design,* vol. 187, p. 108358, 2020.

[21] K. S. Vecchio, O. F. Dippo, K. R. Kaufmann and X. Liu, "High-throughput rapid experimental alloy development (HT-READ)," *Acta Materialia,* vol. 221, p. 117352, 2021.

[22] P. C. Collins, R. Banerjee, S. Banerjee and H. L. Fraser, "Laser deposition of compositionally graded titanium-vanadium and titanium-molybdenum alloys," *Materials Science and Engineering A,* vol. 352, pp. 118-128, 2003.

[23] L. Heng, *Numerical analysis of thermal stress and deformation in multi-layer laser metal deposition process,* 2014.

[24] J. J. Blecher, T. A. Palmer and T. DebRoy, "Solidification Map of a Nickel-Base Alloy," *Metallurgical and Materials Transactions A,* vol. 45A, pp. 2142-2151, 2014.

[25] U. S. Bertoli, G. Guss, S. Wu, M. J. Matthews and J. M. Schoenung, "In-situ characterization of laser-powder interaction and cooling rates through high-speed imaging of powder bed fusion additive manufacturing," *Materials and Design,* vol. 123, pp. 385-396, 2017.

[26] H. L. Wei, G. L. Knapp, T. Mukherjee and T. DebRoy, "Three-dimensional grain growth during multi-layer printing of a nickel-based alloy Inconel 718," *Additive Manufacturing,* vol. 25, pp. 448-459, 2019.

[27] S. M. Kelly and S. L. Kampe, "Microstructural Evolution in Laser-Deposited Multilayer Ti-6Al-4V Builds: Part I. Microstructural Characterization," *Metallurgical and Materials Transactions A,* vol. 35A, pp. 1861-1867, 2004.

[28] D. Kumar, G. Shankar, K. G. Prashanth and S. Suwas, "Control of texture and microstructure in additive manufacturing of stainless steel 316 L," *Journal of Alloys and Compounds,* vol. 976, p. 173040, 2024.

[29] N. Raghavan, R. Dehoff, S. Pannala, S. Simunovic, M. Kirka, J. Turner, N. Carlson and S. S. Babu, "Numerical modeling of heat-tranfer and the influence of process parameters on tailoring the


Distribution Statement A: Approved for public release. Distribution is unlimited.

grain morphology of IN718 in electron beam addtive manufacturing," *Acta Materialia,* vol. 112, pp. 303-314, 2016.

[30] N. Raghavan, S. Simunovic, R. Dehoff, A. Plotkowski, J. Turner, M. Kirka and S. Babu, "Localized melt-scan strategy for site specific control of grain size and primary dendrite arm spacing in electron beam additive manufacturing," *Acta Materialia,* vol. 140, pp. 375-387, 2017.

[31] R. R. Dehoff, M. M. Kirka, W. J. Sames, H. Bilheux, A. S. Tremsin, L. E. Lowe and S. S. Babu, "Site specific control of cystallographic grain orientation through electron beam additive manufacturing," *Materials Science and Technology,* vol. 31, no. 8, pp. 931-938, 2015.

[32] M. E. Parker, D. J. Horton and K. J. Wahl, "Tribocorrosion Behavior of 2205 Duplex Stainless Steel in Sodium Chloride and Sodium Sulfate Environments," *Tribology Leters,* p. 70, 2022.

[33] F. Leijon, S. Wachter, Z. Fu, C. Körner, S. Skjervold and J. Moverare, "A novel rapid alloy development method towards powder bed additive manufacturing, demonstrated for binary Al-Ti, -Zr and -Nb alloys," *Materials & Design,* vol. 211, p. 110129, 2021.

[34] Q. Jia, P. Rometsch, S. Cao, K. Zhang and X. Wu, "Towards a high strength aluminum alloy development methodology for selective laser melting," *Materials and Design,* vol. 174, p. 107775, 2019.

[35] A. I. Mardare, A. Savan, A. Ludwig and A. D. Wieck, "High-throughput synthesis and characterization of anodic oxides on Nb-Ti alloys," *Electrochimica Acta,* vol. 54, pp. 5973-5980, 2009.

[36] P. Jemmely, S. Mischler and D. Landolt, "Electrochemical modeling of passivation phenomena in tribocorrosion," *Wear,* vol. 237, pp. 63-76, 2000.


Distribution Statement A: Approved for public release. Distribution is unlimited.

# Appendix

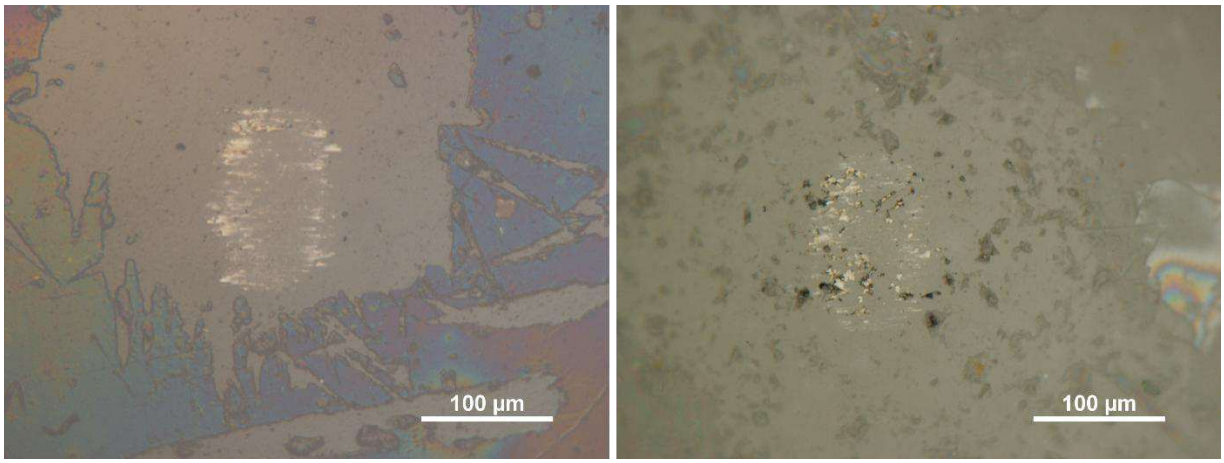



Figure 13. Alumina counterbody surface after sliding experiment showing minimal plastic deformation.


Distribution Statement A: Approved for public release. Distribution is unlimited.

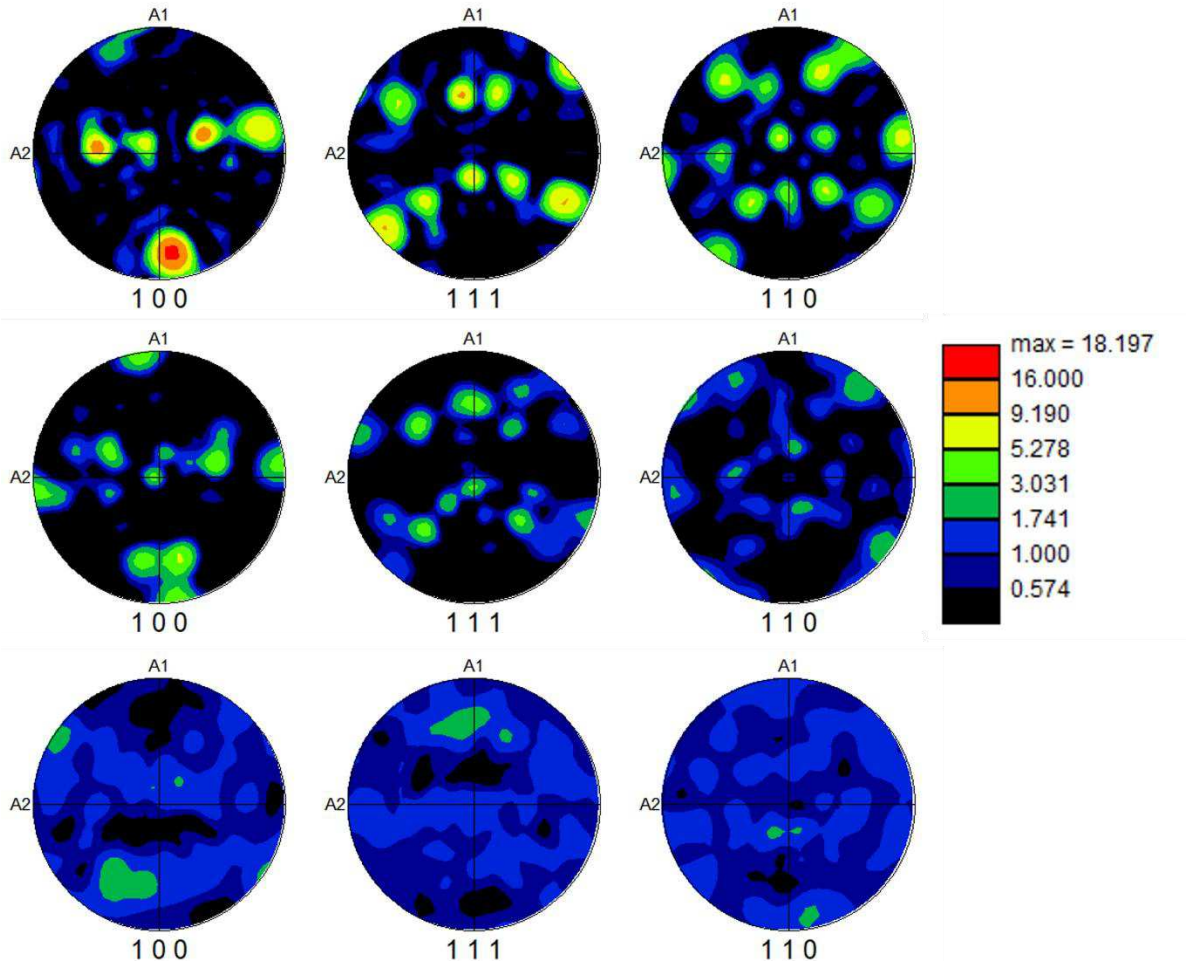



Figure 14. Pole figures for EBSD scan showing clear <100> texture is present in thin wall AM sample.


Distribution Statement A: Approved for public release. Distribution is unlimited.